Surface & Coatings Technology 386 (2020) 125468

Contents lists available at ScienceDirect

Surface & Coatings Technology

journal homepage: www.elsevier.com/locate/surfcoat

Sliding wear behaviour of WC-Co reinforced NiCrFeSiB HVOAF thermal spray coatings against WC-Co and Al_2O_3 counterbodies

J. Pulsford[a], F. Venturi[a], S. Kamnis[b], T. Hussain[a,*]

[a] Faculty of Engineering, University of Nottingham, Nottingham NG7 2RD, UK
[b] Castolin Eutectic - Monitor Coatings Ltd, North Shields NE29 8SE, UK

ARTICLE INFO

Keywords:
HVOF thermal spray
Sliding wear
WC-Co
NiCrFeSiB

ABSTRACT

NiCrFeSiB alloys reinforced with WC-Co are potentially useful composite coating materials for use in applications in which resistance to sliding wear, hot corrosion and high temperature is required. Furthermore these materials offer an advantage over WC-Co and WC-CoCr coatings in applications where a more ductile coating is required. A powder feedstock containing a 50/50 mixture of WC-Co/NiCrFeSiB was sprayed by a HVOAF (high velocity oxy-air fuel) thermal spray torch, which was developed by Monitor Coatings Castolin Eutectic for internal diameter applications, with two sets of spray parameters with the overall gas flowrate entering the torch changed. The powder feedstock and sprayed coatings were characterised using SEM imaging, XRD and measurement of mechanical properties such as microhardness and indentation fracture toughness. The specific wear rates of the coatings were measured when testing the coatings against WC-Co and Al_2O_3 counterbodies and it was determined that the coating sprayed at the higher gas flowrate wore out less against both counterbody materials, due to its superior microhardness. Tests against the Al_2O_3 counterbody led to increased material loss of both coatings in comparison to testing against WC-Co. This was due to the wear of the Al_2O_3 ball throughout the test leading to an increase in contact area between the coating and counterbody.

1. Introduction

NiCrSiB or NiCrFeSiB alloys are useful materials for use in applications in which resistance to wear, corrosion and heat is required, such as in boilers of coal fuelled power plants or gas turbines [1]. However this material is currently not widely used in many engineering applications due to the material's low hardness in comparison to other more common coating materials such as cermet and ceramic coatings [2]. WC-Co/NiCrSiB blended powder has significant advantages over WC-Co or even WC-Co-Cr when a more ductile coating is required in engineering applications. The addition of reinforcement particles, such as cermets like WC-Co to the powder feedstock has been previously shown to improve the mechanical properties of the final coating, with the hardness of pure NiCrSiB and 50% NiCrSiB/ 50% WC by weight coatings sprayed by atmospheric plasma spraying (APS) being shown to increase from 10.082 ± 0.720 GPa to 14.293 ± 1.393 GPa with the addition of the reinforcing particles. Furthermore Young's modulus was seen to increase from 232 ± 19 GPa to 291 ± 15 GPa with the addition of the WC [3]. Consequently, the improvement in these properties has been shown to greatly improve the sliding resistance of the coating. The sliding wear resistance of WC-Co/NiCrSiB coatings sprayed by HVOF (High velocity oxy–fuel) thermal spraying with varied mass fractions from 0% wt. WC-Co to 30% WC-Co was measured at a 10 N load against a WC-Co counterbody and it was determined that the wear resistance improved as the mass fraction of cermet in the powder feedstock increased, with the specific wear rate of the coating being lowered by about 38% when 30% wt. WC-Co was included [4]. The ability to improve NiCrFeSiB coatings with added reinforcing particles has been recognised by the engineering community, with powder manufacturers providing mixed powder feedstocks for use in coating applications. Composite coatings of WC-Co/NiCrSiB have been sprayed by HVOF thermal spray in a number of studies, with the tribological studies focusing on the erosive wear of the coating against alumina at room temperature and at 450 °C with coatings with a microhardness of 1223 HV with a porosity of below 0.5% being achieved [5,6].

Techniques such as plasma spraying, laser cladding, detonation gun, cold spray and HVOF have been successfully used to apply these coatings [5,7–9]; however, HVOF thermal spray is said to be one of the most promising methods for coating deposition, due to the high particle velocity (≈400–600 m/s) and relatively low flame temperatures in comparison to other methods (< 3000 K) [6]. HVAF (High velocity air fuel) thermal spraying is a technique that involves the use of

* Corresponding author.
E-mail address: tanvir.hussain@nottingham.ac.uk (T. Hussain).

https://doi.org/10.1016/j.surfcoat.2020.125468
Received 25 November 2019; Received in revised form 31 January 2020; Accepted 11 February 2020
Available online 18 February 2020

compressed air instead of pure oxygen, alongside the fuel for combustion with the said advantages being a lower flame temperature and a higher in-flight particle velocity compared to HVOF thermal spraying resulting in less unwanted decarburisation when spraying cermet powders [10]. In recent years, changes in legislation led to a keen interest in developing a thermal spray process to apply coatings on internal surfaces, known as ID (internal diameter) thermal spraying. Due to the line of sight nature of thermal spray processes, ID thermal spraying provides additional challenges, particularly when applying coatings in parts with a small ID, such as having to deal with a short stand-off distance and barrel length. To tackle these issues, a new generation of ID thermal spray torches has been developed with much smaller dimensions than traditionally used industry standards which are able to apply coatings at much smaller stand-off distances [11,12]. Currently little is known regarding the effects of spraying a mixed powder feedstock with such a system. From an economics point of view, the blended WC-Co/NiCrSiB has nearly twice the deposition efficiency compared to that of WC-Co or WC-Co-Cr in internal diameter HVOF thermal spray torches.

In this study, a commercially bought composite powder feedstock consisting of a 50:50 by weight mixture of WC-Co and NiFeCrSiB particles was sprayed using a next generation ID HVOAF (High velocity oxy-air fuel) thermal spray system developed by Castolin Eutectic-Monitor Coatings Ltd. (North Shields, UK), utilising both air and oxygen alongside the fuel for combustion. Two sets of spray parameters were used with a varied gas flowrate used in order to affect the amount of heating undergone by the powder particles within the flame, in order to confirm which parameter set produces coatings more suited to providing resistance against sliding wear. The microstructure, mechanical properties and sliding wear resistance of the coatings against Al_2O_3 and WC-Co counterbodies were investigated.

2. Experimental

2.1. Feedstock materials and HVOAF thermal spray coating deposition

A commercially available powder feedstock consisting of 50/50 wt % WC-Co /NiCrFeSiB by weight (AMPERIT® 560.090) was acquired from H.C. Starck (Munich, Germany). The nominal powder size range stated by the manufacturer was 45/5 μm. The composition of the WC-Co powder is 83/17% wt., and the NiCrFeSiB particles are stated by the manufacturer to have an approximate composition of 13–17% Cr, 3.9–4.9% Si, 2.4–4.6% Fe, 3–3.9% B, 0.6–1.2% C with the balance being Ni, all in wt. %. Coatings were deposited using a HVOAF torch developed by Castolin Eutectic-Monitor Coatings (North Shields, United Kingdom) that has been used in other studies [11,13–15] onto AISI 416 stainless steel (12–14% Cr, 1.25% Mn, 0.15% C, 0.15% S, 0.6% Mo, 0.06% P, 1% Si in weight %) disks of diameter 38.1 mm and thickness of 6 mm. Prior to deposition, the substrate materials were grit blasted and degreased with acetone in order to improve coating/substrate bonding. The coatings were sprayed using two different sets of spray parameters, denoted NiSF_HF (Nickel self-fluxing high flowrate) and NiSF_LF (Nickel self-fluxing low flowrate) with the gas flowrates into the torch for each being 500 L/min and 150 L/min respectively. The samples were sprayed in a normal HVOF spray setup used for the coating of outer surfaces with a stand-off distance of 100 mm.

2.2. Characterisation of powder feedstock and coatings

Prior to coating deposition, the powder size range of the mixture was measured using a LS230 laser diffraction powder sizer (Beckmann Coulter Inc., CA, USA). The phase composition of the coatings and powder feedstock was measured by X-ray diffraction using a Siemens D500 (Siemens, Munich, Germany) utilising Cu K_α radiation (1.5406 Å) in the $20^\circ \leq 2\theta \leq 90^\circ$ range, with a step size of 0.02° and a dwell time of 4 s. Cross sections of the coatings were prepared by sectioning the sample with a SiC cutting wheel followed by grinding and polishing down to a 1 μm diamond finish. The morphology and microstructure of the powder and coating cross sections were examined using a Jeol 6490LV scanning electron microscope (SEM) operated in high vacuum mode and utilising both secondary (SE) and backscattered electron (BSE) imaging (Jeol Ltd., Tokyo, Japan). The porosity and the relative volume percentage of WC-Co splats within the coating's microstructure were measured using image analysis software (Image J, NIH, USA) [16]; 5 images were considered for each coating with the overall mean percentage being presented along with the standard error.

The microhardness of the coatings was measured on the prepared polished cross sections using a Vickers microhardness indenter (Buehler, Illinois, USA) using a load of 300 gf and a dwell time of 10 s. The indentation fracture toughness of the samples was measured by indenting the cross section of the coating samples with a Vickers hardness indenter using a load of 2.5 kgf in order to produce small horizontal cracks propagating from the edge of the indentation. Only cracks in the direction parallel to the coating/substrate interface were considered, as it has been previously shown in HVOF thermal spray coatings that the fracture toughness is lowest in this direction [17]. The lengths of these cracks and indent size were measured using optical microscopy (Nikon, Japan) and the indentation fracture toughness K_{IC} was determined using the relationship described by Evans and Wilshaw [18]:

$$K_{Ic} = 0.079\left(\frac{P}{a^{3/2}}\right)\log\left(\frac{4.5a}{c}\right) \quad (1)$$

where P is the applied indentation load (N), a is the indentation half diagonal (m) and c is the crack length from the indent centre (m). This expression is only valid when $0.6 \leq c/a \leq 4.5$; all measurements of c and a were determined to fit within this range for all samples measured. For all microhardness and fracture toughness measurements, the mean values from 6 indentations are presented alongside the standard error.

2.3. Dry sliding wear testing

Unlubricated sliding wear tests were carried out at room temperature using a Ducom rotary ball on disc microtribometer (Ducom, The Netherlands) with a load of 10 N, sliding distance of 500 m and sliding speed of 0.16 m/s used. In order to assess performance of the system when sliding against ceramic and a like on like cermet material, Al_2O_3 and WC-Co balls supplied by Dejay Ltd. (Launceston, UK) with a diameter of 6 mm were used as the counterbody. The frictional force during each test was measured by the instrument, from which the coefficient of friction μ could be calculated to investigate the effect of the change of counterbody material on the frictional response exhibited by the system. All tests were carried out on a coating surface polished down to a 1 μm finish achieved by using SiC grinding papers down to a 15.3 μm grit size, followed by polishing against 6 μm and 1 μm diamond pads. The wear track diameter was set at 10 mm for all tests and each test was repeated twice on fresh samples to improve the reliability of the results, with the mean and range being presented. Contact surface profilometry (Taylor Hobson Ltd., UK) was used to measure the surface roughness (R_a) of the polished coating surface prior to testing, with the R_a of the polished coatings being found to lie in the range of 0.02–0.05 μm. The R_a of the counterbody materials was stated by the manufacturer to be < 0.02 μm.

2.4. Characterisation of worn surfaces

The specific wear rate of the coatings was measured by using a surface profilometer (Taylor Hobson Ltd., UK) to measure the cross-sectional area of the wear scar perpendicular to the direction of the counterbody movement in 4 places. These were averaged and then multiplied by the wear track circumference to provide the volume of

material lost during the test. This value can then be divided by the load multiplied by the total sliding distance of the test in order to provide the specific wear rate of each worn sample [13,19].

Wear of the spherical counterbodies during the test would result in a near flat surface, and by using the assumption that this represents the removal of a spherical cap of material, the following expressions can be used to calculate of volume of material lost by the counterbody:

$$d = r - \sqrt{(r^2 - a^2)} \tag{2}$$

$$\Delta V = \pi d^2 \left(r - \frac{d}{3} \right) \tag{3}$$

where ΔV represents the volume loss, d the height of the cap, r the ball radius and a the radius of the wear scar. The contact surface of the worn Al_2O_3 counterbody was then imaged by SEM, with a carbon coating of approximately 15 nm thickness added in order to promote conductivity.

The worn surfaces of the coatings were analysed using SEM with SE and BSE imaging modes, in order to assess the wear mechanism and condition of the coatings. Raman spectroscopy was employed to characterise oxides present within the wear scar using a LabRAM HR spectrometer (Horiba jobin YVON, Japan) modified by the addition of an automated xyz stage (Märzhäuser, Germany). The instrument was calibrated using a standard Si (100) reference band at 520.7 cm^{-1} and the Rayleigh line at 0 cm^{-1}. A laser with a wavelength of 659.41 nm with a 300 μm pinhole was utilised with a 10% laser filter used to prevent damaging the sample. The individual spectra were collected for 20 s and were repeated 3 times in order to improve the signal to noise ratio. Following data correction the spectra were corrected by applying linear baseline subtraction in order to remove effects of fluorescence.

3. Results

3.1. Characterisation of feedstock powder and deposited coatings

A SE SEM image of the powder feedstock, alongside a BSE SEM image of the powder cross sections are shown in Fig. 1. The particles of WC-Co are roughly spherical in shape, with an exterior covered in grains of WC. The mean carbide grain size was measured as approximately 3 μm. Cross sectional BSE images show the WC phase embedded in the Co binder phase with a darker contrast, alongside porosity visible inside the particles, typical of agglomerated and sintered powders. The NiCrFeSiB particles are the larger spherical grey particles, seen to be larger in size than the WC-Co particles. Cross sectional BSE SEM images indicated these particles are non-porous, with two distinct phases being visible; measurements from EDX point scans of these two phases are shown in Table 1. The spots with the darker contrast within the Ni phase particles were found to be Cr rich with Ni content falling from around 70.9 wt% in the surrounding areas to 29.5 wt% in the Cr rich regions.

Table 1
Measurements from EDX point scans of the cross section of a Ni alloy particle.

Location (all in wt%)	C	Si	Cr	Fe	Ni	B
Point 1	6.0	4.6	14.8	3.7	70.9	–
Point 2	11.3	1.5	35.8	2.8	29.5	19.1

SEM SE and BSE images of the cross sections of both coatings are presented in Fig. 2. Both coatings have densely packed structures with no signs of cracking, with good adhesion to the substrate, as can be seen due to a total lack of any crack or delamination along the interface. The NiSF_HF and NiSF_LF coatings had a measured thickness of (518 ± 11) μm and (576 ± 8) μm. The splats of the Ni alloy and WC-Co particles can be seen throughout the microstructure, with many Ni alloy splats still retaining their spherical shape. The diameter of 10 spherical Ni alloy splats seen from cross sectional BSE images of the coatings were measured, with the average diameter in the NiSF_HF and NiSF_LF coatings found to equal (41 ± 11) μm and (37 ± 7) μm respectively; however, this may differ depending on how the sample was prepared. The Cr rich areas that can be observed on the cross section of the Ni alloy particles in Fig. 1 can also be observed within the coating microstructure within some Ni alloy splats. Thin string like phases with a bright contrast, marked on Fig. 2 with red arrows, can be seen positioned between splats of Ni alloy throughout the microstructure of both coatings. An EDX line scan across one such site was carried out with the results displayed in Fig. 3. The areas scanned in the darker contrast area were found to contain large element weight percentages of Ni (> 60%) with little measured W and Co (< 15%). The scanned points in the brighter contrast region were still seen to contain measureable amounts of Ni, with a spot roughly in the centre of the feature measured to contain an elemental weight percentage of approximately 15% Ni. This may indicate that a form of mixing between the two separate powders has taken place; however, whether or not this is due to the EDX generation region being larger than the measured phase is the reason for the detection of Ni cannot be confirmed.

XRD diffractograms of the powder feedstock and sprayed coatings are displayed in Fig. 4. The phases detected that can be attributed to the WC-Co powder are WC (PDF 00-051-0939) and Co (PDF 00-015-0806) as seen in other work [20], with the Ni particles displaying a more complex phase composition. Aside from the presence of Ni (PDF 00-001-1258), a number of silicide species were detected including $Ni_{31}Si_{12}$ (PDF 00-024-0524), $FeSi_2$ (PDF 03-065-2795), CrSi (PDF 00-051-1356) and $Cr_{6.5}Ni_{2.5}Si$ (PDF 00-016-0037). The presence of silicides has also been detected in other studies working with similar self-fluxing Ni alloys [21]. The presence of borides Ni_4B_3 (PDF 00-012-0417) and Cr_2B_3 (PDF 01-089-3534) was also detected within the powder feedstock. The XRD diffractograms of the as sprayed coatings reveal the presence of a broad hump between approximately

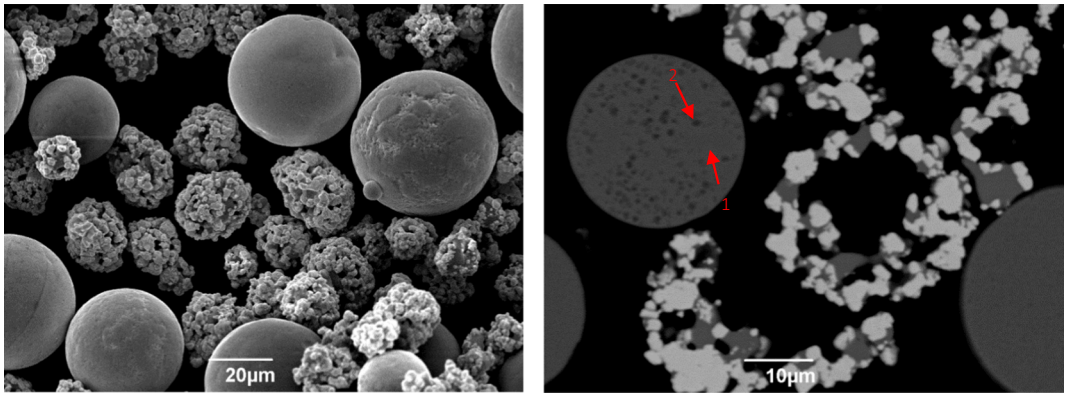

Fig. 1. SEM secondary electron image of the composite feedstock powder. EDX point scans were carried out on the marked areas.

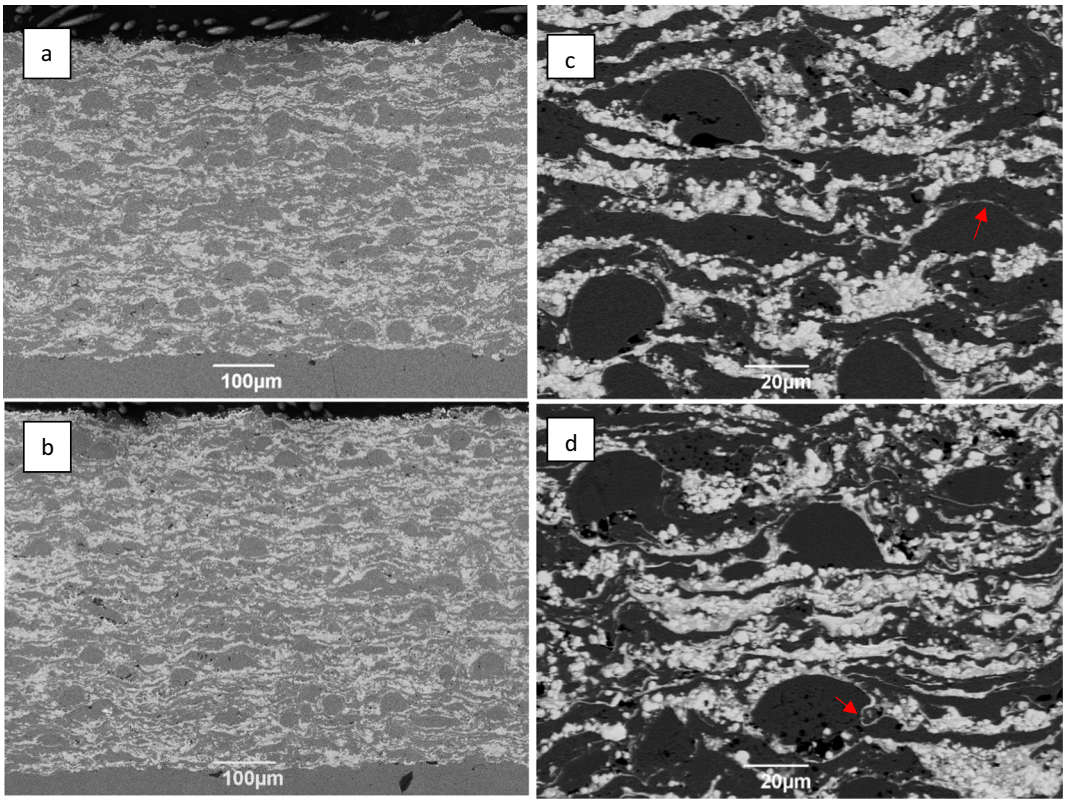

Fig. 2. (a,b) SEM secondary electron images of the NiSF_HF and NiSF_LF coatings. (c,d) BSE images of the coating microstructures. Intersplat phases are marked on the images with a red arrow. (For interpretation of the references to colour in this figure legend, the reader is referred to the web version of this article.)

$37^\circ < 2\theta < 50^\circ$ possibly indicating the formation of amorphous or nanocrystalline phases during the spray process. The peaks attributed to minor phases contained within the Ni alloy can be seen to have reduced in intensity in both sprayed coatings in comparison to the powder feedstock; likely these crystalline phases that were detected in the powder that can no longer be seen formed a solid solution during the spray process and had insufficient time to fully recrystallise when the particle was quenched on impact with the substrate. No W_2C phase or elemental W was detected in the as sprayed coatings, meaning little to no decarburisation of the WC phase occurred during spraying [19].

The microhardness, indentation fracture toughness and measured porosity of the as sprayed coatings are presented in Table 2. NiSF_HF was found to have a higher hardness than the NiSF_LF coating, with values of 926 ± 83 and 762 ± 112 respectively. The fracture toughness of the NiSF_HF coating was measured at 4.5 ± 0.2 $MPa.m^{0.5}$ and the NiSF_LF coating at 4.8 ± 0.5 $MPa.m^{0.5}$; therefore the toughness of the two coatings is likely similar when taking the margin of error into account. A small degree of porosity can be seen in both coatings but appears more prominent in the NiSF_LF coating with pores normally found to be situated on the interface between Ni alloy and WC-Co splats. This was confirmed by the porosity measurements, which showed the NiSF_HF coating having a very low measured porosity of (0.3 ± 0.1)% and the NiSF_LF coating with a measured (1.3 ± 0.2)%.

The relative volume percentage of splats of WC-Co was analysed for each coating, with the NiSF_HF and NiSF_LF coatings being measured with (30.3 ± 2.1)% and (30.9 ± 1.1)% respectively, with the remainder being either Ni alloy phase or porosity. This indicates that the amounts of the hard WC-Co particles within the microstructure are very similar for both coatings.

3.2. Dry sliding wear testing

The specific wear rates of the coatings against both counterbody materials are displayed in Fig. 5. The NiSF_HF coating wore at a rate of 5.00×10^{-7} mm^3/Nm against the WC-Co counterbody and 1.10×10^{-6} mm^3/Nm vs. the Al_2O_3 counterbody. Meanwhile the NiSF_LF coating wore at a rate of 5.43×10^{-7} mm^3/Nm against the WC-Co counterbody and 1.23×10^{-6} mm^3/Nm vs. the Al_2O_3 counterbody. Both coatings were seen to wear significantly more when tested against the Al_2O_3 counterbody in comparison to WC-Co, with the specific wear rate increasing by 120% and 127% for the NiSF_HF and NiSF_LF coatings vs. Al_2O_3 in comparison to WC-Co. The specific wear rates of the counterbodies were also measured; in all tests the WC-Co counterbodies were found to undergo negligible wear, with no flat surface forming on the contact surface of the ball with this material. In contrast the Al_2O_3 counterbodies were seen to visibly wear during the test with a flat surface forming on the ball. The mean specific wear rates of the Al_2O_3 balls tested vs. the NiSF_HF and NiSF_LF coatings were measured as $(4.85 \pm 0.95) \times 10^{-7}$ mm^3/Nm and $(1.36 \pm 0.42) \times 10^{-7}$ mm^3/Nm respectively.

The coefficient of friction measured in each wear tests vs. distance travelled by the counterbody against both materials are displayed in Fig. 6. Against both counterbody materials, the break-in period occurs for approximately the first 100 m travelled with large variations in coefficient of friction μ measured; however, while μ is seen to remain relatively constant at a value of about 0.6 for the remaining distance when tested against Al_2O_3, it can be seen to decrease during the test in the wear tests vs. WC-Co for both coatings from a maximum of about 0.7 down to below 0.5. The change in μ throughout each test was found to be similar for the NiSF_HF and NiSF_LF coatings, suggesting little to no difference in the wear mechanisms taking place in the wear of each coating. The final value of the coefficient of friction was seen to be greater for both samples tested against the Al_2O_3 counterbody compared to WC-Co.

Low magnification secondary electron SEM images of the wear tracks produced from the sliding wear tests against both counterbody

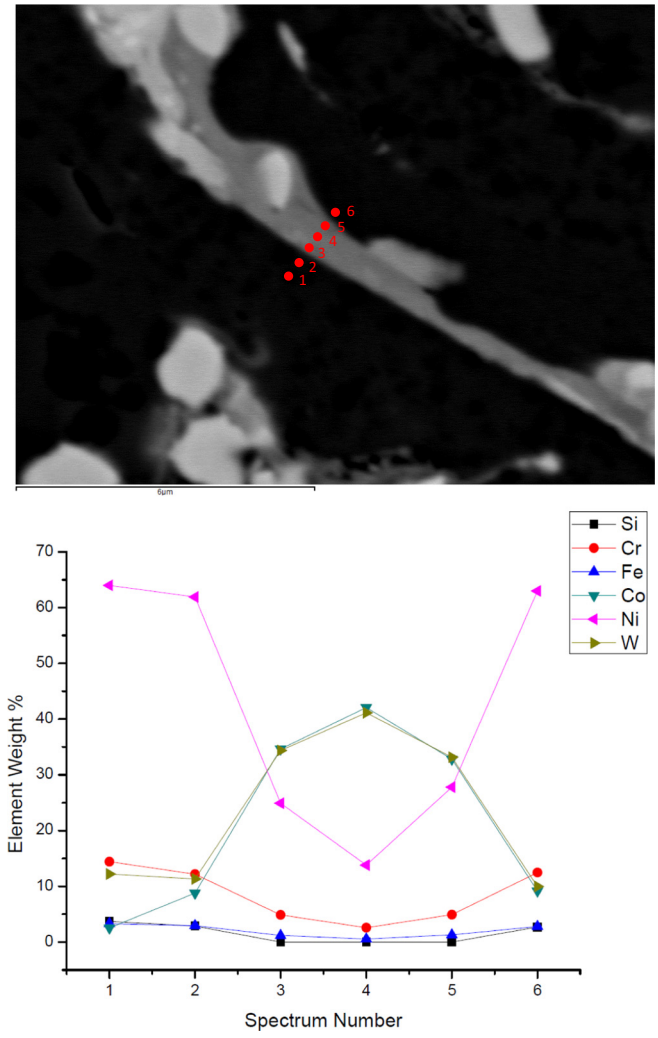

Fig. 3. EDX line scan across the intersplat phase marked in Fig. 2.

materials are shown in Fig. 7. The width of the observed wear track was measured at approximately 171 ± 3 μm and 276 ± 9 μm for the NiSF_HF and LF coatings against the WC-Co counterbody and 329 ± 16 μm and 456 ± 7 μm for the NiSF_HF and LF coatings against the Al_2O_3 counterbody.

Table 2
Microhardness, fracture toughness and porosity of the two coatings.

Sample	Microhardness (HV0.3)	Fracture toughness K_{IC} ($MPa.m^{0.5}$)	Porosity (%)
NiSF_HT	926 ± 83	4.5 ± 0.2	0.3 ± 0.1
NiSF_LT	762 ± 112	4.8 ± 0.5	1.3 ± 0.2

SE and BSE SEM images of the worn surface of the coatings tested against the WC-Co counterbodies are presented in Fig. 8. Some small cracks were found between areas of under deformed, spherical shaped splats of Ni alloy particles; these are marked on the images with a red arrow. Small pores can be visible on the worn surface, likely to be sites where material pullout of WC occurred and these are displayed on the image with circles. Scratches parallel to the direction of counterbody movement can be observed on the surface of both coatings, covering WC-Co rich and Ni rich areas. This suggests an abrasive wear mechanism may be one of the processes taking place in this tribological system, characterised by the presence of these grooves visible on the worn surface, formed by ploughing of a harder material through softer areas of the microstructure. Areas of material with a darker contrast can be seen on the SEM images where cracks perpendicular to the direction of the movement of the counterbody are present. EDX point scans in these areas detected a large concentration of oxygen, meaning these areas are likely oxides. These areas can be seen lying over WC-Co and Ni alloy splats, indicating no preferential location for formation. Small bright dots can be seen on the surface, with a similar contrast in BSE but a much smaller size to the WC grains; these are likely tungsten rich debris scattered across the worn surface produced from pulled out WC grains or abrasive wear of said phase.

Images of the surface worn vs. the Al_2O_3 counterbody are displayed in Fig. 9. Similar features can be seen to those observed of the worn surfaces from the wear tests carried out against WC-Co, with abrasive scratches, small cracks between Ni alloy splats and oxidised areas all visible. Tungsten rich debris can also again be seen on the surface. Overall, for both counterbody materials, little difference between the worn surfaces on the two coatings can be observed. Examples of the measured surface profiles of the worn surfaces of both coatings are displayed in Fig. 9. The wear tracks produced from wear against the Al_2O_3 counterbody can be seen to have a larger width than the wear scar formed in the tests against WC-Co, with a measured width of approximately 0.4 mm and 0.36 mm in comparison to 0.26 mm and 0.2 mm for the NiSF_HF and NiSF_LF coatings tested against WC-Co.

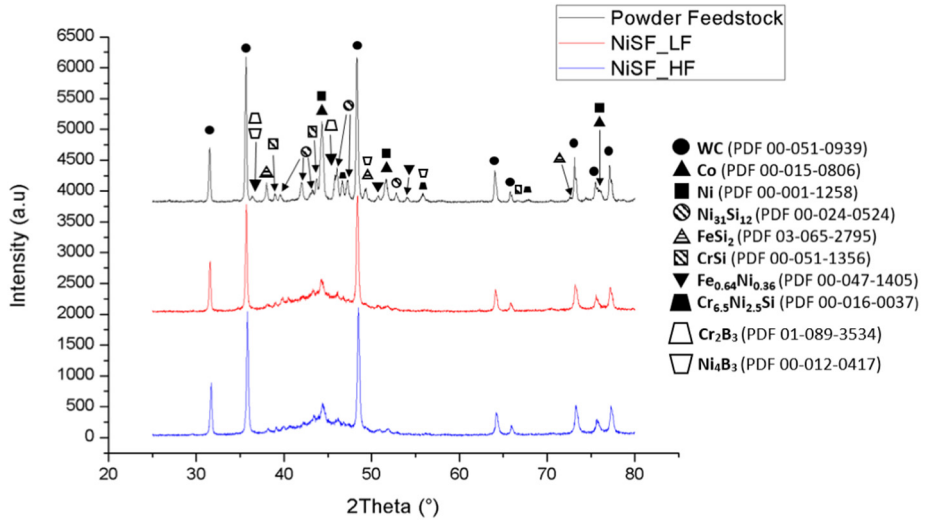

Fig. 4. XRD diffractograms of the powder feedstock and as-sprayed coatings.

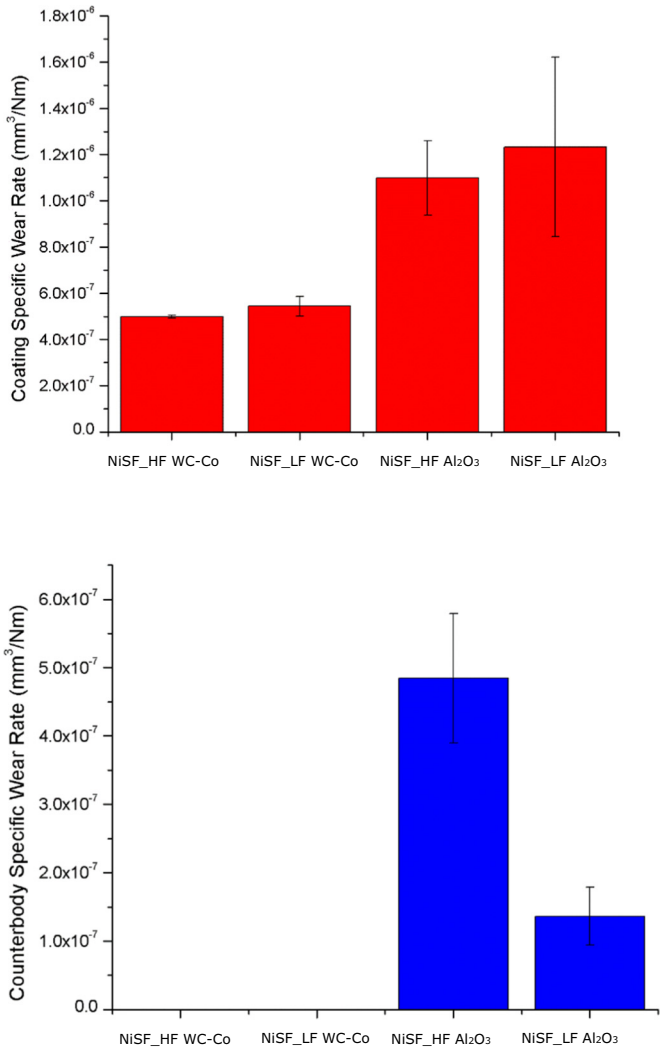

Fig. 5. Specific wear rates of the coatings and counterbodies.

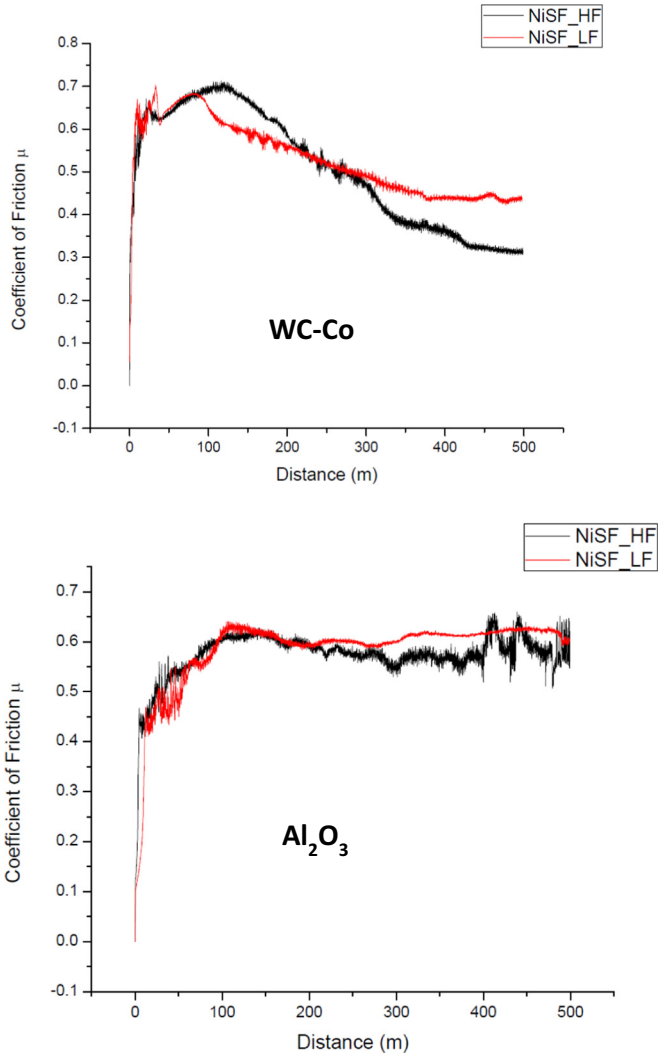

Fig. 6. Coefficient of friction vs. distance travelled for the wear tests against the WC-Co and Al_2O_3 counterbodies.

Raman spectra gathered from oxidised regions on the worn surfaces of the NiSF_HF coating tested against both counterbody materials are presented in Fig. 10. No difference was observed between the oxides formed on the two coatings with peaks attributed to WO_3, $CoWO_4$ and a Ni-W based oxide detected, with Raman spectra of the pure materials being used as the reference from other studies [22,23]. Furthermore, the Raman spectra reveal little difference between the oxides forming in the wear tests against both counterbody materials.

Secondary and backscattered electron images of the contact surface of an Al_2O_3 ball used in the wear test against the NiSF_HF coating are displayed in Fig. 11. Low magnification images reveal the presence of a "smoothed out area" which displays a brighter contrast than the bulk material in BSE imaging. EDX point scan in these areas, marked by a red dot, detected the significant presence of elements present in the coating material such as W, Co and Ni meaning material transfer from the coating took place during the test. The presence of cracks in the regions surrounding the circular worn cap can also be observed. Higher magnification images of the region marked by a red box reveal a worn surface characteristic of an area in which brittle fracture mechanisms have occurred, similar to that seen in another work [24]. BSE imaging in this region also shows material with a brighter contrast embedded into the Al_2O_3 surface, with EDX point scans again implying this material originating from the coating. Due to the lack of wear of the WC-Co counterbodies during testing, these materials were not imaged.

4. Discussion

4.1. Powder and coating characterisation

It is likely the selected spray parameters resulted in favourable in-flight characteristics in general for the WC-Co particles, but less so for the Ni alloy. SEM images of the powder feedstock in Fig. 1 reveal that the Ni alloy particles vary in size, with the diameter of the particles imaged seen to vary between 23 and 45 μm. Assuming a consistent spherical morphology, the difference in volume between the smallest and largest Ni alloy particles imaged would vary by almost 750%. As a result, it is likely that the temperature of Ni alloy particles in-flight would vary to a large degree due to the differences in heat energy required to sufficiently heat up and promote the particle melting required in HVOF thermal spray processes. Furthermore a greater kinetic energy is required for heavier Ni alloy particles to reach the high in-flight velocity required to ensure sufficient flattening on impact with the substrate, making it likely that larger particles of the Ni alloy will not only have lower in-flight temperatures, but lower velocities too in comparison with smaller particles of the same material. These under deformed splats can be seen to be formed from larger Ni alloy particles, which either did not have sufficient in-flight velocity or temperature to ensure high plastic deformation on impact. It has been previously determined in other studies carried out using in-flight particle diagnostic

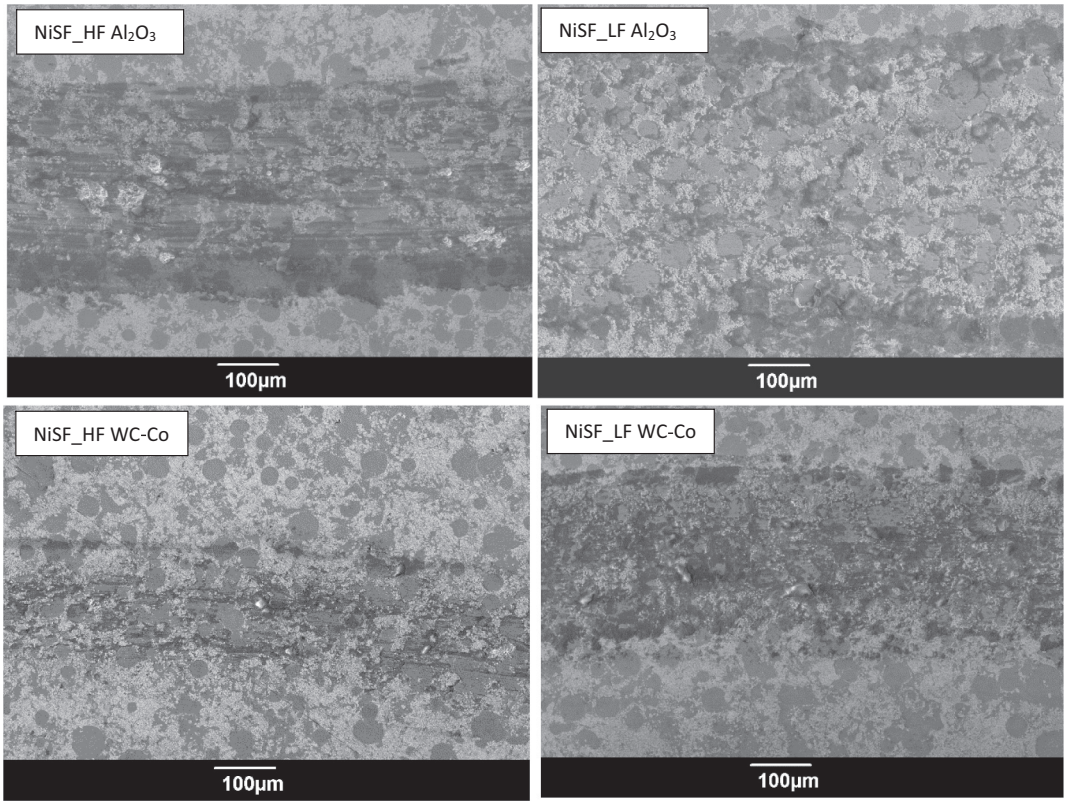

Fig. 7. Low magnification SE SEM images of the worn surfaces of the coatings tested against both counterbody materials. Note the greater width of the tracks worn against the Al_2O_3 counterbody.

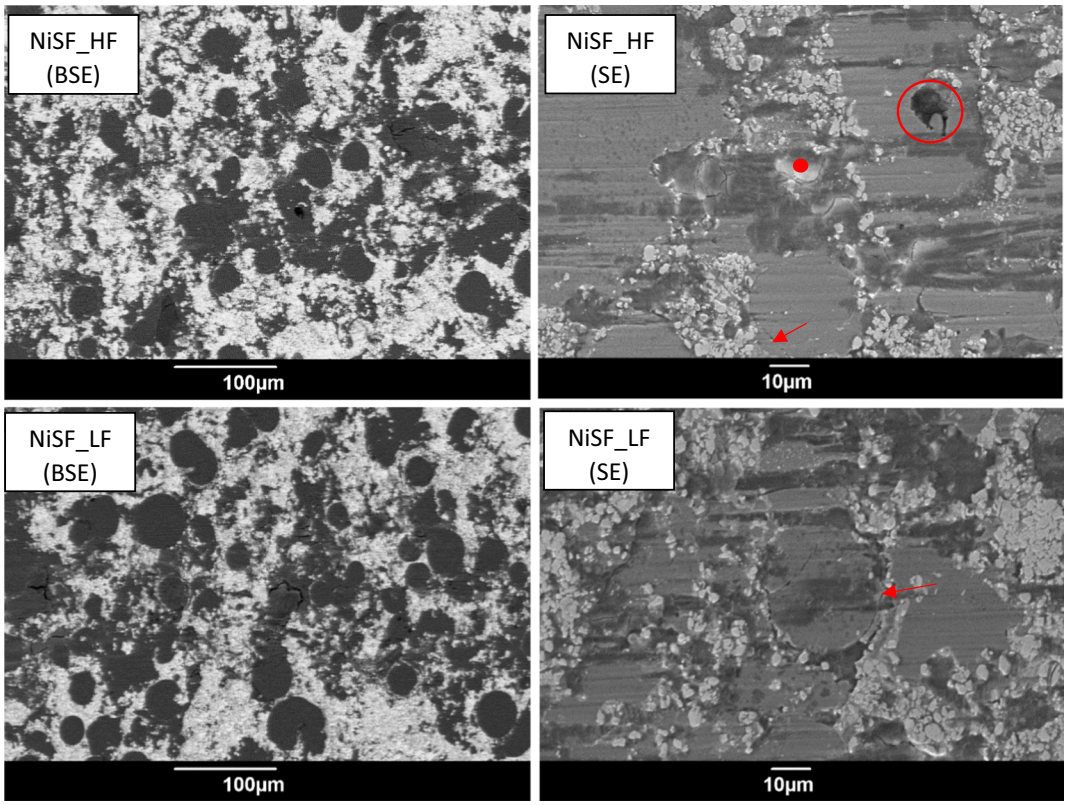

Fig. 8. SEM BSE and SE images of the worn surfaces of the coatings tested against the WC-Co counterbody. Cracking originating from the interphase between the cermet and Ni alloy splats and example areas of oxidised material are marked with arrows and dots respectively.

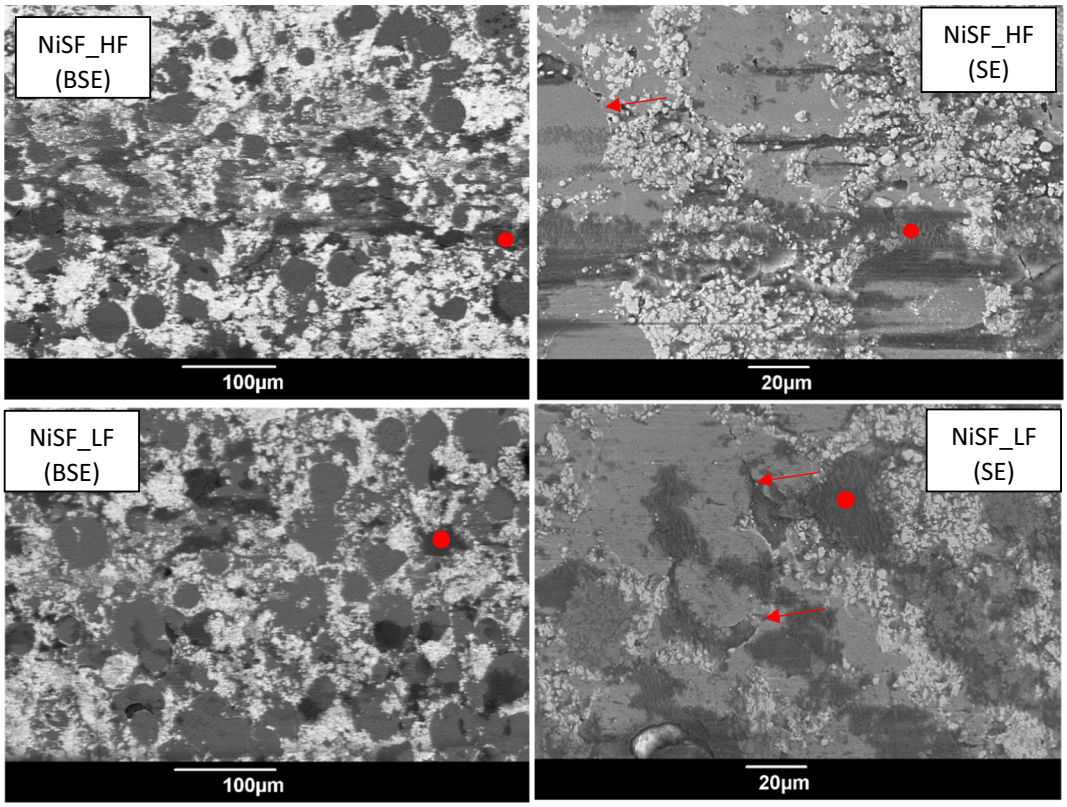

Fig. 9. SEM BSE and SE images of the worn surfaces of the coatings tested against the Al_2O_3 counterbody. Cracking originating from the interphase between the cermet and Ni alloy splats and example areas of oxide are marked with an arrow and dot respectively.

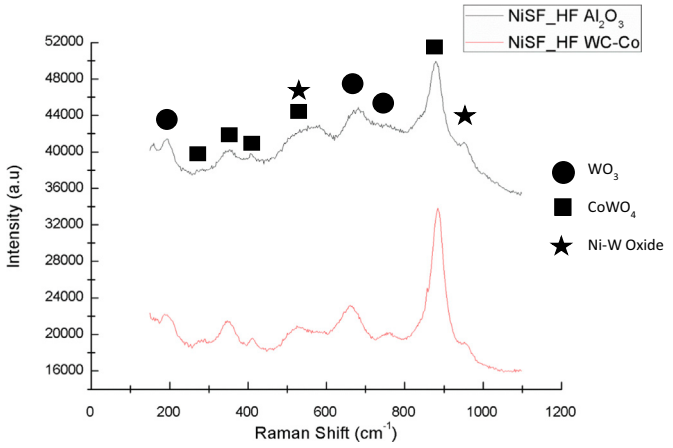

Fig. 10. Raman spectra measured from the worn surface of the NiSF_HF coating worn vs. both counterbody materials.

and CFD simulation methods that insufficient flattening of the powder feedstock on impact with the substrate will produce more porous coatings [25,26]. The coating sprayed under conditions leading lower particle velocities NiSF_LF was measured to have a higher porosity than the NiSF_HF coating. Insufficient acceleration of the Ni alloy particles as a result of the lower gas flowrate into the torch results in insufficient plastic deformation of the particles on impact with the substrate and as a result will lead to a more porous coating. Furthermore increased porosity has been shown to lead to a reduced microhardness in HVOF thermal sprayed coatings [27], providing a likely explanation for the increased microhardness of the NiSF_HF coating. The relative volume percentage of the microstructure taken up by splats of the harder WC-Co powder is unlikely to account for the difference in microhardness between the two coatings due to the similarity in the relative volume of this phase. The indentation fracture toughness was measured to be higher for the NiSF_LF coating; however, the error was also larger making it likely the fracture toughness of the coatings does not vary significantly.

Due to their generally smaller size and porous and hollow structure, the WC-Co particles possess a higher surface area to volume ratio than the larger solid Ni alloy particles, likely increasing the efficiency of heat transfer from the hot gases into the WC-Co particles in flight. Meanwhile in contrast, the Ni alloy particles were found to have a homogenous spherical shape with a smooth non-porous outer surface, which combined with their generally larger size would result in much slower heating rates for the Ni alloy than the WC-Co particles during the spray process. The specific heat capacities of the two materials were estimated using empirical relationships from other sources [28,29] at a range of temperatures and it was observed that the specific heat capacity of the Ni alloy particles at 0.46 kJ/kg.K is almost twice as large as for WC-Co at 0.24 kJ/kg.K, meaning the effect of particle size on heating rate is even more pronounced for NiCrFeSiB. This difference in particle heating rates means it may be extremely challenging to optimise spray parameters in order to achieve the best out of both materials in this mixture, as raising the flame power to sufficiently melt the NiCrFeSiB alloy particles would increase the likelihood of overheating the WC-Co particles, resulting in unfavourable decarburisation of WC. Changing the size of the powder feedstock by reducing the amount of larger Ni alloy particles may allow easier optimisation of spray parameters for HVOAF thermal spray deposition. With this powder feedstock, this could be achieved by employing the use of a sieve with a 40 μm grating size to remove the large Ni alloy particles. However there is a chance that removing the larger Ni alloy particles would lead to a difference in composition between the WC-Co and Ni alloy phases within the final coating; this may have an effect on the final properties of the coating but this is beyond the scope of this work.

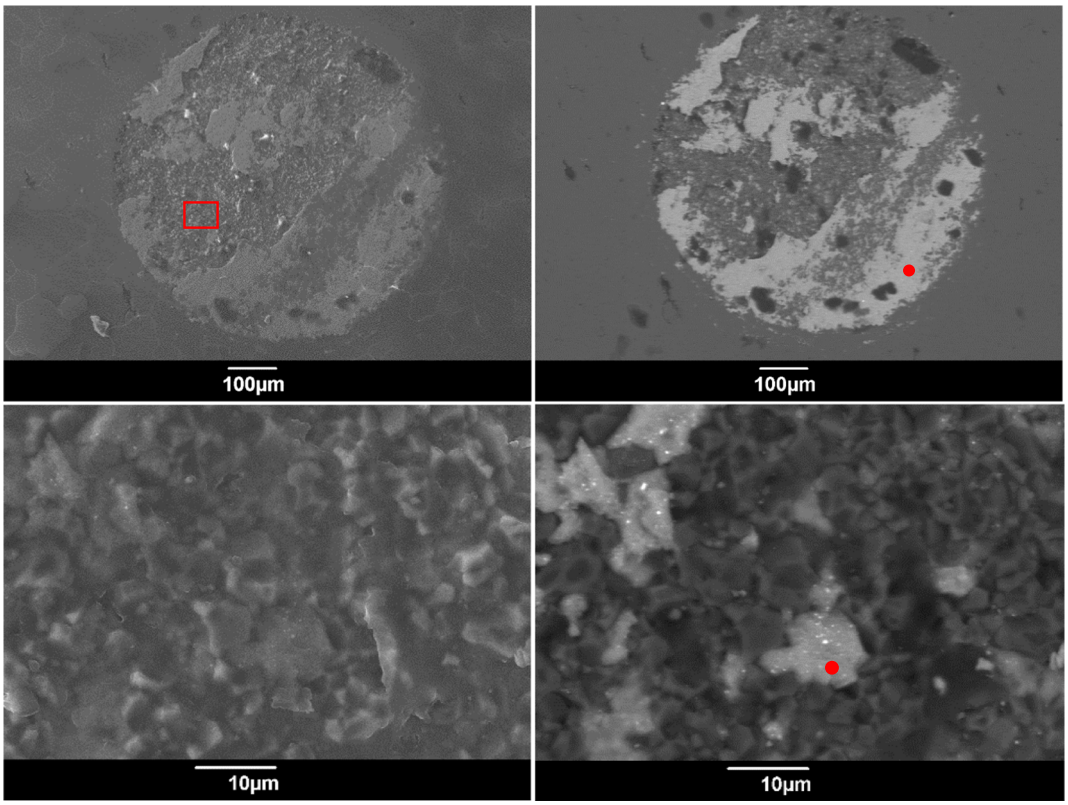

Fig. 11. SE and BSE SEM images of the worn surface of the Al_2O_3 ball. Spots marked with a red circle indicate positions at which EDX point scans were performed and the red box shows the approximate location of the higher magnification images. (For interpretation of the references to colour in this figure legend, the reader is referred to the web version of this article.)

4.2. Dry sliding wear behaviour

In both sliding wear tests, the coating sprayed at the higher flame temperature NiSF_HF was found to wear at a slower rate than the other coating. This better resistance to sliding wear can likely be related to the greater microhardness of this coating, a conclusion reached in other studies regarding sliding wear of HVOF thermal sprayed coatings [30]. It is likely the mechanism of wear was very similar for both coatings for each counterbody material, as the change of the friction coefficient against distance travelled is alike for both coatings. Furthermore, on inspection of the worn surfaces of both coatings in Figs. 7 and 8, similar features are observed such as signs of WC grain pull-out, scratch marks and cracks originating from around the perimeter of spherical Ni alloy splats. SEM images of the coating cross section in Fig. 2 show porosity can be present in these areas and using principals of linear elastic fracture mechanics, it is likely that stresses concentrate in the material at areas of porosity, resulting in cracks propagating from these areas.

A significant difference in measured specific wear rate was seen when the coatings were worn against the two different counterbody materials, with both coatings wearing at a much greater rate against Al_2O_3. Raman spectroscopy on the worn surfaces of the coatings tested against both counterbody materials revealed the presence of WO_3, $CoWO_4$ and Ni-W oxides. Pullout of hard WC phase leads to hard material getting trapped between the counterbody and coating surface, resulting in the abrasion marks that can be seen across the coating surface in Fig. 8. These trapped particles can begin to react with atmospheric oxygen, due to being heated by the friction generated by the contact between the counterbody and coating surface under load, likely leading to the formation of WO_3 or $CoWO_4$ oxides in a similar manner to that described in other work with cermet HVOF coatings [31]. Abrasion of the Ni alloy splats results in Ni rich debris being produced, which may oxidise in a similar manner to the other oxides that have been seen to form.

In the tests against both coatings, the Al_2O_3 counterbodies underwent wear resulting in a flat surface forming at the point of contact between the ball and coating surface. In contrast the WC-Co balls were seen to undergo little to no wear, with the balls retaining their spherical shape, due to this material's higher hardness and fracture toughness in comparison to Al_2O_3. In the case of the Al_2O_3 ball the area of the contact surface between the counterbody and coating will increase as the test progresses, due to the round edge of the ball being worn out to form a flat surface. A larger contact surface between the counterbody and coating may increase the coating wear, as the larger contact surface would allow more pulled out abrasive materials to get trapped between counterbody and coating leading to an increase in wear by abrasion in the system [32]. Embedded coating particles can be observed on the worn surface of the Al_2O_3 ball in Fig. 11, providing evidence for this explanation.

The behaviour of the coefficient of friction displayed in Fig. 6, throughout the test was observed to differ for each counterbody material, implying the response of the worn coating and counterbody material may be different. The formation of $CoWO_4$ and WO_3 tribofilms on the worn surface of the coatings has previously been shown to act as a solid lubricant and lower the coefficient of friction [33,34]. The double oxide $CoWO_4$ is composed of CoO and WO_3 which have significant ionic potential differences; a characteristic which has been previously shown to promote antifriction properties [33,35].

The presence of these oxides was detected on the worn surface of the coatings tested against both counterbody materials; however, the coefficient of friction was not seen to reduce in the tests against the Al_2O_3 counterbody. The wear of the Al_2O_3 was seen to occur via a brittle fracture mechanism in a manner characteristic of severe wear in ceramic materials. The occurrence of brittle fracture can result in increased frictional forces, due to the fractures providing an additional

mechanism for the dissipation of energy at the area of the sliding contact [36], countering the potential lubricating effect provided by the oxides formed by tribo-chemical processes. However, in a wear coupling in which the counterbody material is seen not to undergo severe wear, such as when tested against WC-Co, it appears the lubricating effect provided by the formation of oxides on the worn surface can be achieved.

The coating with the lowest wear against both counterbody materials, NiSF_HF, had a measured specific wear rate of $(4.99 \pm 0.06) \times 10^{-7}$ mm^3/Nm against the WC-Co counterbody and $(1.10 \pm 0.16) \times 10^{-6}$ mm^3/Nm against Al_2O_3. For comparison, unlubricated sliding wear tests investigating the wear of WC-CoCr coatings sprayed by liquid fuelled HVOF thermal spray (JP-5000, Praxair, USA) and HVAF (high velocity air-fuel) thermal spray (M3, UniqueCoat Technologies, USA) at a 10 N load against a 6 mm diameter Al_2O_3 ball (5000 m sliding distance, 0.1 m/s sliding speed) were found to result in coating specific wear rates of approximately 6×10^{-8} mm^3/Nm for the HVOF sprayed coating and 3×10^{-8} mm^3/Nm for the HVAF thermal spray coating [31]. The WC-CoCr coatings were both found to have a microhardness of > 1200 HV0.3, with the HVAF coating having a slightly higher hardness; it is likely that this increase in hardness can explain the difference in performance between the WC-Co/NiCrFeSiB composite coatings and benchmark WC-CoCr coatings. While the specific wear rates of the WC-Co/NiCrFeSiB coatings studied in this work are of an order of magnitude higher than WC-CoCr coatings, the wear these coatings suffered is in the orders of magnitude classed as mild wear [36] meaning they show good potential as wear resistant coatings for low load sliding wear applications.

5. Conclusion

A composite powder feedstock containing a 50/50 mixture of WC-Co/NiCrFeSiB was sprayed under two different spray conditions, with the total gas flowrate into the torch set at 500 L/min (NiSF_HF) and 150 L/min (NiSF_LF) to vary the microstructure of the coatings. The coatings were exposed to unlubricated sliding wear testing to understand their wear mechanisms against WC-Co and Al_2O_3 counterbodies. The following conclusions can be made:

- A larger amount of porosity was present in the NiSF_LF coating, with the NiSF_HF coating having a very low measured porosity of (0.3 ± 0.1)% and the NiSF_LF coating with a measured porosity of (1.3 ± 0.2)%. In combination, the coating sprayed at the higher total gas flowrate NiSF_HF was found to have a greater microhardness than the NiSF_LF coating with values of 926 ± 83 and 762 ± 112 respectively, while fracture toughness is likely similar for the two coatings. This could be due to the in-flight particles, in particular the larger Ni alloy particles having too low in-flight velocity to flatten sufficiently on impact with the substrate at the lower gas flowrate into the torch. This effect would be more significant for larger particles, meaning for this powder feedstock the use of a 40 μm sieve to remove these largest particles prior to spraying could improve the coating microstructure and therefore properties.
- The NiSF_HF coating sprayed at the higher total gas flowrate was found to suffer less material loss during the wear tests against both the WC-Co and Al_2O_3 counterbodies than the NiSF_LF coating, due to its higher hardness. The main mechanism of wear was found to be similar for both coatings, with the pullout of hard phases in the coating microstructure leading to abrasion of the coating surface. Patches of oxidised material can be seen on the worn surfaces of both coatings.
- Both coatings suffered a higher degree of wear when tested against the Al_2O_3 counterbody in comparison to the WC-Co counterbody. This was due to the wear of the Al_2O_3 ball throughout the test leading to an increase in contact area between the coating and counterbody, leading to a greater amount of wear due to abrasion mechanisms.

CRediT authorship contribution statement

J. Pulsford: Investigation, Formal analysis, Writing - original draft, Writing - review & editing. **F. Venturi:** Supervision, Formal analysis, Writing - review & editing. **S. Kamnis:** Supervision, Project administration, Resources, Conceptualization. **T. Hussain:** Supervision, Project administration, Writing - review & editing.

Declaration of competing interest

The authors declare that they have no known competing financial interests or personal relationships that could have appeared to influence the work reported in this paper.

Acknowledgement

This work was supported by the Engineering and Physical Sciences Research Council [grant number EP/L016362/1]; in the form of an EngD studentship and industrial funding from Castolin Eutectic-Monitor Coatings Ltd. Furthermore we would like to thank Mr. Kerem Derelizade for help with the Raman spectroscopy measurements, and the Nanoscale and Microscale Research Centre (nmRC) at the University of Nottingham for the use of SEM equipment. In addition, we would like to thank Dr. Acacio Rincon Romero for help with the XRD analysis.

References

[1] V.H. Hidalgo, J.B. Varela, A.C. Menéndez, S.P. Martínez, High temperature erosion wear of flame and plasma-sprayed nickel-chromium coatings under simulated coal-fired boiler atmospheres, Wear 247 (2001) 214–222, https://doi.org/10.1016/S0043-1648(00)00540-8.
[2] M.J. Tobar, C. Álvarez, J.M. Amado, G. Rodríguez, A. Yáñez, Morphology and characterization of laser clad composite NiCrBSi-WC coatings on stainless steel, Surf. Coat. Technol. 200 (2006) 6313–6317, https://doi.org/10.1016/j.surfcoat.2005.11.093.
[3] N. Serres, F. Hlawka, S. Costil, C. Langlade, F. MacHi, Microstructures and mechanical properties of metallic NiCrBSi and composite NiCrBSi-WC layers manufactured via hybrid plasma/laser process, Appl. Surf. Sci. 257 (2011) 5132–5137, https://doi.org/10.1016/j.apsusc.2010.11.062.
[4] I. Conciatu, C. Ciubotariu, E. Secosan, D. Frunzaverde, C. Campian, Microstructure and wear behaviour of self-fluxing alloy coatings reinforced by WC-Co, IOP Conf. Ser. Mater. Sci. Eng, 444 2018.
[5] A.S. Praveen, J. Sarangan, S. Suresh, B.H. Channabasappa, Optimization and erosion wear response of NiCrSiB/WC-Co HVOF coating using Taguchi method, Ceram. Int. 42 (2016) 1094–1104, https://doi.org/10.1016/j.ceramint.2015.09.036.
[6] M.R. Ramesh, S. Prakash, S.K. Nath, P.K. Sapra, B. Venkataraman, Solid particle erosion of HVOF sprayed WC-Co/NiCrFeSiB coatings, Wear 269 (2010) 197–205, https://doi.org/10.1016/j.wear.2010.03.019.
[7] A.S. Praveen, J. Sarangan, S. Suresh, J. Siva Subramanian, Erosion wear behaviour of plasma sprayed NiCrSiB/Al2O3 composite coating, Int. J. Refract. Met. Hard Mater. 52 (2015) 209–218, https://doi.org/10.1016/j.ijrmhm.2015.06.005.
[8] P.R. Reinaldo, A.S.C.M. D'Oliveira, NiCrSiB coatings deposited by plasma transferred arc on different steel substrates, J. Mater. Eng. Perform. 22 (2013) 590–597, https://doi.org/10.1007/s11665-012-0271-7.
[9] L. Peng, Preparation and tribological properties of NiCrBSiC reinforced laser alloying layer, Tribol. Trans. 56 (2013) 697–702, https://doi.org/10.1080/10402004.2013.782619.
[10] L. Jacobs, M.M. Hyland, M. De Bonte, Study of the influence of microstructural properties on the sliding-wear behavior of HVOF and HVAF sprayed WC-cermet coatings, J. Therm. Spray Technol. 8 (1999) 125–132, https://doi.org/10.1361/105996399770350656.
[11] J. Pulsford, F. Venturi, Z. Pala, S. Kamnis, T. Hussain, Application of HVOF WC-Co-Cr coatings on the internal surface of small cylinders: effect of internal diameter on the wear resistance, Wear. 432–433 (2019) 202965, https://doi.org/10.1016/j.wear.2019.202965.
[12] C. Lyphout, S. Bjorklund, Internal diameter HVAF spraying for wear and corrosion applications, J. Therm. Spray Technol. 24 (2015) 235–243, https://doi.org/10.1007/s11666-014-0195-x.
[13] J. Pulsford, S. Kamnis, J. Murray, M. Bai, T. Hussain, Effect of particle and carbide grain sizes on a HVOAF WC-Co-Cr coating for the future application on internal surfaces: microstructure and wear, Proc. Int. Therm. Spray Conf, 2017.
[14] V. Katranidis, S. Kamnis, B. Allcock, S. Gu, Effects and interplays of spray angle and stand-off distance on the sliding wear behavior of HVOF WC-17Co coatings, J.

Therm. Spray Technol. 28 (2019) 514–534, https://doi.org/10.1007/s11666-019-00831-x.
[15] B. Allcock, S. Gu, S. Kamnis, Nozzle for a Thermal Spray Gun and Method of Thermal Spraying, EP2411554B1, (2013).
[16] J. Schindelin, E.T. Arena, B.E. DeZonia, M.C. Hiner, K.W. Eliceiri, C.T. Rueden, A.E. Walter, ImageJ2: ImageJ for the next generation of scientific image data, BMC Bioinf. 18 (2017) 1–26, https://doi.org/10.1186/s12859-017-1934-z.
[17] M.M. Lima, C. Godoy, P.J. Modenesi, J.C. Avelar-Batista, A. Davison, A. Matthews, Coating fracture toughness determined by Vickers indentation: an important parameter in cavitation erosion resistance of WC-Co thermally sprayed coatings, Surf. Coat. Technol. 177–178 (2004) 489–496, https://doi.org/10.1016/S0257-8972(03)00917-4.
[18] A.G. Evans, T.R. Wilshaw, Quasi-static solid particle damage in brittle solids-I. Observations analysis and implications, Acta Metall. 24 (1976) 939–956, https://doi.org/10.1016/0001-6160(76)90042-0.
[19] P.H. Shipway, D.G. McCartney, T. Sudaprasert, Sliding wear behaviour of conventional and nanostructured HVOF sprayed WC-Co coatings, Wear 259 (2005) 820–827, https://doi.org/10.1016/j.wear.2005.02.059.
[20] D. Stewart, P.H. Shipway, D.G. McCartney, Microstructural evolution in thermally sprayed WC-Co coatings: comparison between nanocomposite and conventional starting powders, Acta Mater. 48 (2000) 1593–1604, https://doi.org/10.1016/S1359-6454(99)00440-1.
[21] L. Gil, M.H. Staia, Microstructure and properties of HVOF thermal sprayed NiWCrBSi coatings, Surf. Coat. Technol. 120–121 (1999) 423–429, https://doi.org/10.1016/S0257-8972(99)00494-6.
[22] X. Xing, Y. Gui, G. Zhang, C. Song, CoWO4 nanoparticles prepared by two methods displaying different structures and supercapacitive performances, Electrochim. Acta 157 (2015) 15–22, https://doi.org/10.1016/j.electacta.2015.01.055.
[23] S.H. Lee, H.M. Cheong, N.G. Park, C.E. Tracy, A. Mascarenhas, D.K. Benson, S.K. Deb, Raman spectroscopic studies of Ni-W oxide thin films, Solid State Ionics 140 (2001) 135–139, https://doi.org/10.1016/S0167-2738(01)00707-X.
[24] T.E. Fischer, Z. Zhu, H. Kim, D.S. Shin, Genesis and role of wear debris in sliding wear of ceramics, Wear 245 (2000) 53–60, https://doi.org/10.1016/S0043-1648(00)00465-8.
[25] T.C. Hanson, C.M. Hackett, G.S. Settles, Independent control of HVOF particle velocity and temperature, J. Therm. Spray Technol. 11 (2002) 75–85, https://doi.org/10.1361/105996302770349005.
[26] M. Li, P.D. Christofides, Multi-scale modeling and analysis of an industrial HVOF thermal spray process, Chem. Eng. Sci. 60 (2005) 3649–3669, https://doi.org/10.1016/j.ces.2005.02.043.
[27] J.R. Davis, Handbook of Thermal Spray Technology, ASM International, 2004.
[28] R. Perry, D. Green, Perry's Chemical Engineering Handbook, 8th ed., McGraw-Hill Education, New York, 2007.
[29] K. Liu, X.P. Li, M. Rahman, X.D. Liu, CBM tool wear in ductile cutting of tungsten carbide, Wear 255 (2003) 1344–1351.
[30] T. Sahraoui, N.E. Fenineche, G. Montavon, C. Coddet, Structure and wear behaviour of HVOF sprayed Cr3C2-NiCr and WC-Co coatings, Mater. Des. 24 (2003) 309–313, https://doi.org/10.1016/S0261-3069(03)00059-1.
[31] G. Bolelli, L.M. Berger, T. Börner, H. Koivuluoto, L. Lusvarghi, C. Lyphout, N. Markocsan, V. Matikainen, P. Nylén, P. Sassatelli, R. Trache, P. Vuoristo, Tribology of HVOF- and HVAF-sprayed WC-10Co4Cr hardmetal coatings: a comparative assessment, Surf. Coat. Technol. 265 (2015) 125–144, https://doi.org/10.1016/j.surfcoat.2015.01.048.
[32] N. Axén, S. Jacobson, S. Hogmark, Influence of hardness of the counterbody in three-body abrasive wear - an overlooked hardness effect, Tribol. Int. 27 (1994) 233–241, https://doi.org/10.1016/0301-679X(94)90003-5.
[33] A. Erdemir, A crystal-chemical approach to lubrication by solid oxides, Tribol. Lett. 8 (2000) 97–102, https://doi.org/10.1023/A:1019183101329.
[34] J.M. Guilemany, J.M. Miguel, S. Vizcaino, F. Climent, Role of three-body abrasion wear in the sliding wear behaviour of WC-Co coatings obtained by thermal spraying, Surf. Coat. Technol. 140 (2001) 141–146, https://doi.org/10.1016/S0257-8972(01)01033-7.
[35] Z. Geng, S. Li, D.L. Duan, Y. Liu, Wear behaviour of WC-Co HVOF coatings at different temperatures in air and argon, Wear. 330–331 (2015) 348–353, https://doi.org/10.1016/j.wear.2015.01.035.
[36] I. Hutchings, P. Shipway, Tribology: Friction and Wear of Engineering Materials, 2nd ed., Elsevier Science & Technology, 2017.